Large Rabi splitting obtained in Ag-WS₂ strong-coupling heterostructure with optical microcavity at room temperature

Bowen Li[1†], Shuai Zu[1†], Zhepeng Zhang[2], Liheng Zheng[1], Qiao Jiang[1], Bowen Du[1], Yang Luo[1], Yongji Gong[3], Yanfeng Zhang[2], Feng Lin[1], Bo Shen[1], Xing Zhu[1], Pulickel M. Ajayan[3] and Zheyu Fang[1,4]*

Manipulation of light-matter interaction is critical in modern physics, especially in the strong coupling regime, where the generated half-light, half-matter bosonic quasiparticles as polaritons are important for fundamental quantum science and applications of optoelectronics and nonlinear optics. Two-dimensional transition metal dichalcogenides (TMDs) are ideal platforms to investigate the strong coupling because of their huge exciton binding energy and large absorption coefficients. Further studies on strong exciton-plasmon coupling by combining TMDs with metallic nanostructures have generated broad interests in recent years. However, because of the huge plasmon radiative damping, the observation of strong coupling is significantly limited at room temperature. Here, we demonstrate that a large Rabi splitting (~300 meV) can be achieved at ambient conditions in the strong coupling regime by embedding Ag-WS₂ heterostructure in an optical microcavity. The generated quasiparticle with part-plasmon, part-exciton and part-light is analyzed with Hopfield coefficients that are calculated by using three-coupled oscillator model. The resulted plasmon-exciton polaritonic hybrid states can efficiently enlarge the obtained Rabi splitting, which paves the way for the practical applications of polaritonic devices based on ultrathin materials.

Keywords: Rabi splitting; strong coupling; transition metal dichalcogenides; optical microcavity; surface plasmons

Introduction

Strong light-matter coupling is crucial for the modern physics, including semiconductor optoelectronics, plasmonics, ultrafast optics, and quantum electrodynamics, etc. When the coherent exchange rate of energy between light and matter is higher than the decay rate, it reaches the strong coupling regime, where two hybrid modes with different energies instead of original independent eigenstates are formed, known as the vacuum Rabi splitting[1]. The strong coupling can result in the for-

mation of half-light, half-matter bosonic quasiparticles called polaritons, which provides a number of possibilities in fascinating advances such as the low-threshold lasing[2], Bose-Einstein condensation[3–5], chemical reactivity tuning[6–8], and optical spin switching[9], etc., and has been widely demonstrated in solid-states, like GaAs quantum dots[10], GaN and ZnO wide-bandgap semiconductors[11,12], and organic polymer materials[13]. However, either the small binding energy of excitons or the strong localization effect of disordered potentials[14], makes traditional semiconductors hardly realize strong-coupled polaritonic

eigenstates at ambient conditions.

Two-dimensional transition metal dichalcogenides (TMDs) have generated broad interests owing to their unique optical and electronic properties[15,16]. Sharp exciton resonances and large exciton binding energies make them excellent candidates for both fundamental and application studies[17]. The monolayer of TMDs gives rise to strongly confined excitons with Bohr radii of ~1 nm and large oscillator strength[18]. Embedding TMD monolayers in an optical microcavity can realize the strong light-matter coupling and generate polaritonic eigenstates, which creates opportunities for engineering the exciton-polariton interaction[19–21]. Though TMD-based polaritons inherit the strong nonlinear interaction and low effective mass properties from the constituent exciton and photon components, most of strong-coupling eigenstates with small Rabi splitting energy were observed in a cryogenic condition and required sophisticated measurement techniques, which impedes the development of practical polaritonic devices.

Surface plasmons (SPs), collective electron oscillations of the metallic nanostructure, can tightly confine the incident light into nanoscale[22], which results in a strongly enhanced local field with ultrasmall mode volume and hence provides an advantaged platform for strong coupling investigations[23–28]. In the past decades, many attentions have been paid to plasmon-TMD-exciton systems for studying light-matter interactions, such as plasmon-induced resonance energy transfer[29,30], tunable photoluminance by plasmon[31–37] and Fano resonance[38–40]. The strong plasmon-TMD-exciton coupling also has been investigated[41–48]. However, due to the intrinsic loss of the metal, the quality factor and cooperativity of plasmonic nanocavities are lower than those of conventional optical cavities, and therefore the reliable plasmon-exciton strong coupling has seldom been reported at room temperature. Despite of the Ohmic loss, the strong electric field enhancement and extremely small resonance mode volume[49] indeed make the plasmonic nanostructure an ideal candidate for the strong light-matter coupling investigation.

Here, we report for the first time the observation of strong coupled plasmon-exciton polaritonic hybrid states by embedding Ag-WS$_2$ heterostructure in an optical microcavity under ambient conditions. We demonstrate the hybrid states of optical cavity and plasmonic nanostructure can be further coupled with the exciton of WS$_2$ monolayers, and generate a new kind of quasiparticle with part-plasmon, part-exciton and part-light. The resulted plasmon-exciton polaritonic states can push the Rabi splitting up to 300 meV at the strong coupling regime under the room temperature. Experimental measurements are confirmed by simulations and calculations that based on a three-oscillator model. We believe that the proposed configuration can achieve strong light-matter coupling with a large Rabi-splitting for various flexible device applications based on ultrathin materials in the future.

Results and discussion

The schematic of Ag-WS$_2$ heterostructure is depicted in Fig. 1(a). WS$_2$ monolayers were first transferred to the prepared substrate that consists of a 100 nm Ag mirror and a 30 nm MgF$_2$ spacer. Then Ag nanodisks were fabricated on the WS$_2$ monolayer by using E-beam lithography (EBL) and the following lift-off process. Figure 1(b) shows the scanning electron microscopy (SEM) image of Ag nanodisks with a diameter of 90 nm and thickness of 30 nm on top of WS$_2$ monolayers. Ag was chosen because of its strong plasmon resonance and the relatively low dissipation in the visible range. Photoluminescence (PL) and Raman spectra were measured (See Fig. S1 in the Supplementary Information), which confirms that the WS$_2$ used in the experiment is indeed a monolayer. In Fig. 1(c), we can see the Ag plasmon resonance can be tuned to 610 nm with the designed Ag-MgF$_2$ substrate, and overlaps with the A-exciton absorption peak of WS$_2$ monolayers to realize the plasmon-exciton coupling.

To systematically investigate the exciton-plasmon interaction of this Ag-WS$_2$ heterostructure, a series of Ag nanodisks with different diameters were fabricated on the WS$_2$ monolayers. Reflectivity spectra of bare Ag nanodisks are shown in Fig. S2. The plasmon resonance of Ag nanodisks can be gradually red-shifted from 540 to 700 nm with the diameter increasing, which is in good agreement with finite-difference time-domain (FDTD) simulation results (See Fig. S3 in the Supplementary Information). Figure 1(d) shows reflectivity spectra of Ag-WS$_2$ heterostructures with the Ag disk diameter changed from 85 to 95 nm. The coupling strength in Ag-WS$_2$ heterostructure is determined by the resonance overlap between the plasmon and excitons. For the nanodisk with diameter of 90 nm, the plasmon resonance is close to the WS$_2$ exciton energy, an obvious Rabi splitting can be observed, and two prominent resonance modes are identified as the lower (LPB) and upper plexciton branch (UPB). The Rabi splitting (Ω) between the UPB and LPB on resonance was measured as 85 meV. By comparing this value with the full width at half maximum (FWHM) of the plasmon ($\gamma_{pl} \approx 320$ meV) and exciton ($\gamma_X \approx 50$ meV) modes, the obtained splitting energy ($\Omega \approx 85$ meV) is unsatisfied with the strong coupling criterion[1], where $\Omega < (\gamma_{pl} + \gamma_X)/2$, implying that this plasmon-exciton hybridization is still in the weak coupling regime. The size-dependent dispersion of the Ag-WS$_2$ heterostructure was also calculated by using FDTD solutions. A similar Rabi splitting was observed with the plasmon resonance of the Ag nanodisk getting closer to the exciton of WS$_2$ monolayers at 610 nm, which is consistent well with experimental measurements. (See Fig. S4 in the Supplementary Information).

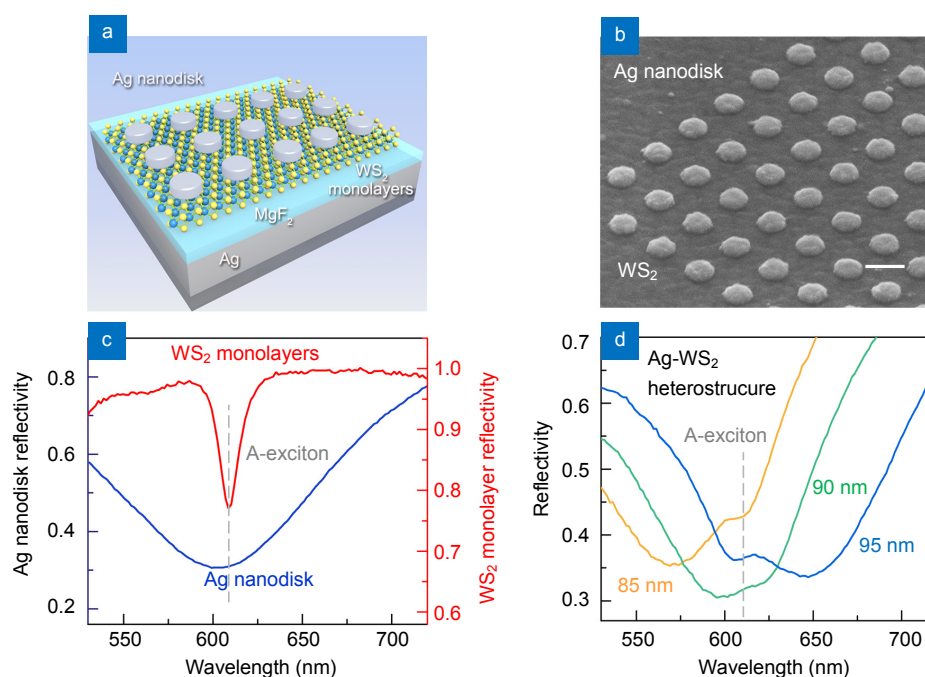In order to enhance the plasmon-exciton coupling, and

Fig. 1 | Characterization of the Ag-WS₂ heterostructure. (**a**) Schematic of the Ag-WS$_2$ heterostructure, where Ag nanodisks were fabricated on WS$_2$ monolayers by EBL. The resonance wavelength of the Ag disk is designed to be resonant with the A-exciton in WS$_2$ monolayers. (**b**) SEM image of the Ag-WS$_2$ heterostructure. The diameter of Ag disk is 90 nm. Scale bar: 150 nm. (**c**) Normalized reflectivity spectra of pure WS$_2$ mono-layers (red line) and bare Ag nanodisks (blue line). The reflectivity spectrum of WS$_2$ monolayers displays a deep dip at ~610 nm, which is consist with the plasmon resonance of Ag nanodisk with diameter of 90 nm. (**d**) Reflectivity spectra of the Ag-WS$_2$ heterostructure with the diameter of Ag nanodisk increased from 85 to 95 nm.

eventually facilitate entering the strong coupling regime, an optical microcavity was manufactured. As shown in Fig. 2(a), by further depositing a 155 nm thickness MgF$_2$ layer and a 20 nm top Ag film onto the fabricated Ag-WS$_2$ heterostructure, we successfully obtained an optical microcavity with the Ag-WS$_2$ heterostructure embedded in MgF$_2$ spacer. Figure 2(b) is the reflection mapping of our cavity sample, and its different layered structures are clearly color distinguished. From the cross section of SEM, the top Ag film, MgF$_2$ spacer, bottom Ag layer, and em-bedded Ag nanodisks can be detailed characterized, as shown in Fig. 2(c).

The optical microcavity was carefully designed to cou-ple well with excitons and plasmons. And the reflectivity spectrum of an empty microcavity was first measured (Fig. S5(a) (solid line) in the Supplementary Information), where a sharp reflection dip centered at 650 nm was achieved, which is resulted from the excitation of the 1st-order of optical cavity mode[50]. This cavity mode was confirmed with the FDTD simulation (Fig. S5(b) (dotted line) in the Supplementary Information), where the elec-tric field intensity distribution (E/E_{in})^2 on the *xoz* plane manifests a huge cavity resonance (Fig. S5(b) in the Sup-plementary Information).

In order to explore the physics origin of strong light-matter coupling, the same optical microcavity with embedded Ag nanodisks (without the WS$_2$ monolayers) was also investigated. The direct plasmon-photon cou-

pling in this Ag-cavity structure leads to two hybridized modes with a maximum bandwidth of 200 meV as shown in Fig. 2(d). The plasmon-photon coupling strength can be effectively tuned with different sized Ag nanodisks. In comparison with the pure plasmon mode of Ag nanodisk, the Ag-cavity structure shows a higher electric field en-hancement and a narrower resonance bandwidth[51], which provides a better option for the further strong coupling study.

Figure 2(e) gives reflectivity spectra of optical microcavity with the Ag-WS$_2$ heterostructure embedded in the MgF$_2$ layer. Three different hybridized modes, as the upper branch, middle branch, and lower branch were generated. By increasing the size of Ag nanodisk, the up-per branch gradually approaches the A-exciton of the WS$_2$ monolayers, the middle branch shifts away from the A-exciton and gradually approaches the microcavity mode, while the lower branch shifts away from the A-exciton mode. Black solid lines in Fig. 2(e) trace the dispersion of three branches, and anticrossing trends are found for the Ag disk size changed from 90 to 110 nm, which indicates the strong coupling happened in this Ag-WS$_2$ heterostructure that associated with the optical microcavity. To highlight these three branches, the spec-trum for 110 nm and 95 nm in Fig. 2(e) are expanded and shown in Figs. 2(f) and 2(g), respectively. When the di-ameter of Ag nanodisk is 110 nm, the weak coupling was observed, only two hybrid modes can be distinguished.
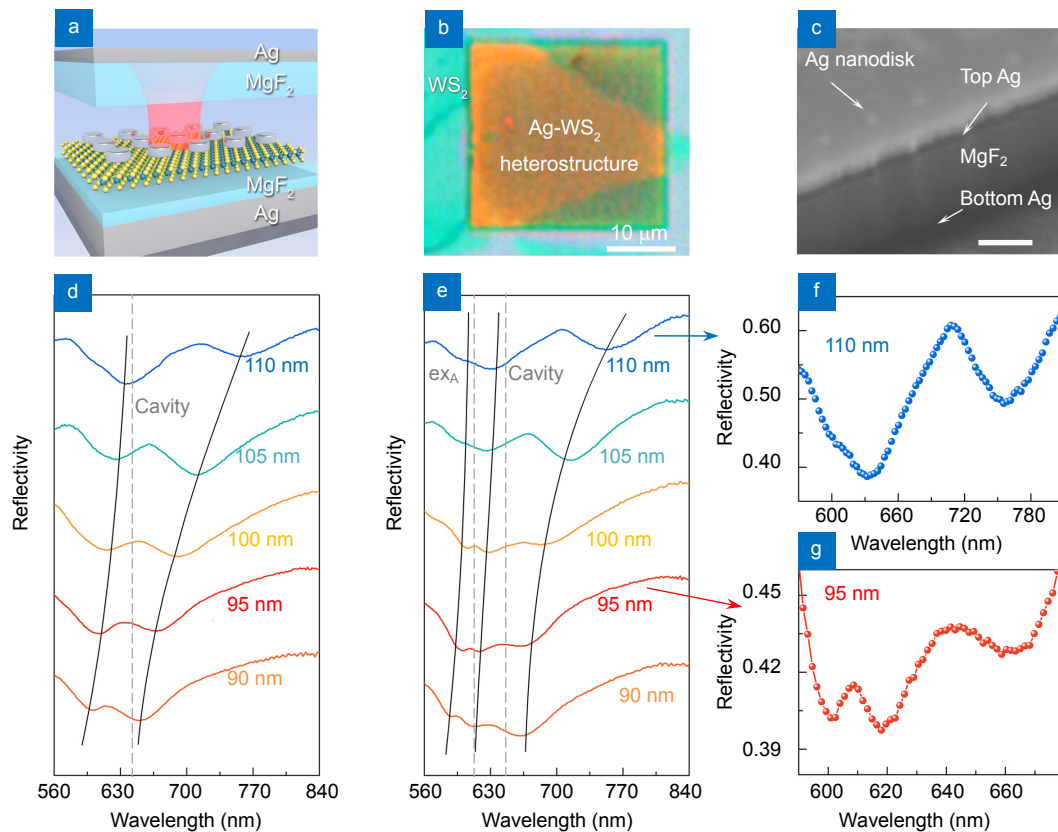
Fig. 2 | Strong coupling in the Ag-WS₂ heterostructure with an optical microcavity. (**a**) Schematic of the optical microcavity with an embedded Ag-WS₂ heterostructure. The microcavity is manufactured in a sandwich structure with a 100 nm-thick Ag layer at the bottom, a 185 nm-thick MgF₂ layer in the middle, and a 20 nm-thick Ag layer on the top. (**b**) The reflectivity spectral mapping of the Ag-WS₂ heterostructure with optical microcavity. Here the diameter of Ag nanodisk is 95 nm. Scale bar: 10 μm. (**c**) Cross section view of the Ag-WS₂ heterostructure with optical microcavity at a tilted angle 52°, scale bar is 150 nm. (**d**) Normal-incidence reflectivity spectra of the Ag nanodisk with different sizes directly embedded in the optical microcavity. The Ag nanodisks couple with the optical microcavity, which generates two new hybrid modes with the bandwidth smaller than plasmon resonances of bare Ag nanodisks. (**e**) Normal-incidence reflectivity spectra of the Ag-WS₂ heterostructure with optical microcavity. Three different hybridized modes, as the upper branch, middle branch, and lower branch are observed in reflectivity spectra, which are indicated by black solid lines. Vertical gray dashed lines respectively represents the WS₂ A-exciton energy and the resonance energy of bare optical microcavity. (**f**, **g**) Expanded views of reflectivity spectral features of the heterostructure with the Ag nanodisk diameter of 110 nm (f) and 95 nm (g).

However, for diameter of 95 nm, three pronounced hybridized modes generated by the strong coupling effect corresponding to the upper, middle, and lower branches, which can be clearly observed as shown in Fig. 2(g).

In order to clearly see the mode revolution from the week coupling to strong coupling, FDTD simulations were performed on the same optical microcavity with the bare Ag nanodisk and Ag-WS₂ heterostructure, respectively. The hybridization of the Ag plasmon and cavity mode can be easily distinguished in Fig. 3(a) when the disk size changed from 60 to 130 nm. All resonance dips of measured reflectivity spectra (Fig. 2(d)) correspond to the generated hybrid modes in Fig. 3(a), and the spectral resonance shifting reflects the size-dependent dispersion of each hybrid mode. When the Ag nanodisk changed to the Ag-WS₂ heterostructure, the size-dependent dispersion mapping shows upper, middle and lower branches,

which has a good agreement with measured resonances (Fig. 2(e)) as shown in Fig. 3(b), where the original hybridized states in Fig. 3(a) are coupled with the A-exciton of WS₂ monolayers, and achieve a strong Rabi splitting around 610 nm. In comparison with the Ag nanodisk without microcavity, the electric field of the Ag nanodisk at resonance wavelength 610 nm is enhanced almost 4 times when the microcavity is implemented, as shown in Fig. 3(c), which creates a feasible condition for the plasmon-exciton strong coupling. By extracting the simulated reflectivity for disks with size of 95 nm and 110 nm, as denoted by dashed lines in Fig. 3(b), one can see the output spectra (Fig. 3(d)) present an excellent agreement with the measured reflectivity as Figs. 2(f) and 2(g). Due to the fabrication error of microcavity and the difference of dielectric function between experiment and simulation, the observed splitting energy between cavity and plasmon
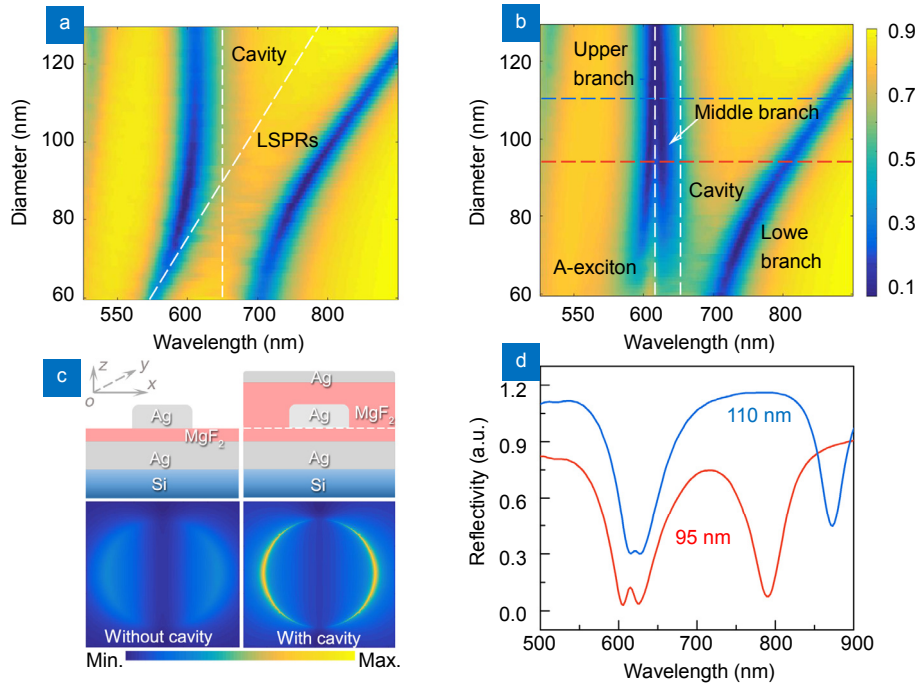
Fig. 3 | FDTD simulation results. (a) Simulated reflectivity spectra of Ag nanodisk embedded in an optical microcavity. White dashed lines represent the resonance wavelength of the empty microcavity (~650 nm). **(b)** Normalized reflectivity spectra of Ag-WS$_2$ heterostructure with the optical microcavity. Three different energy branches are emerged because of the strong coupling among the optical microcavity, surface plasmons and A-exciton of WS$_2$ monolayers. **(c)** Electric field intensity distributions (E/E_{in})^2 on the *xoy* plane of Ag nanodisk with and without microcavity. **(d)** Expanded views of the simulated reflectivity spectral feature for disk size of 110 nm (top line) and 95 nm (bottom line) in (b), respectively.

is smaller than simulation results, which results in a red-shift in simulated low branch compared to the experimental one.

The observed strong coupling of the Ag-WS$_2$ heterostructure with optical microcavity can be further described and analyzed by using coupled oscillator model. Fig. 4(a) is the schematic of plasmon-exciton-cavity three-coupled oscillator model. In the experiment, because the optical microcavity mode is designed far away from the A-exciton of WS$_2$ monolayers, only plasmon-exciton and plasmon-cavity oscillators are connected, and there is no direct coupling between the exciton and cavity photon to generate traditional polaritons.

The Hamiltonian of this three-coupled system can be presented by a matrix as Eq. (1).

$$\hat{H} = \hbar \begin{bmatrix} U_{pl} - i\dfrac{\gamma_{pl}}{2} & g_{MC} & g_X \\[2mm] g_{MC} & U_{MC} - i\dfrac{\gamma_{MC}}{2} & 0 \\[2mm] g_X & 0 & U_X - i\dfrac{\gamma_X}{2} \end{bmatrix}, \quad (1)$$

where γ_{pl}, γ_X and γ_{MC} are the linewidths of plasmon, exciton, and microcavity modes, U_{pl}, U_X, and U_{MC} are the resonance energies of each mode, while g_X and g_{MC} represent plasmon-exciton and plasmon-microcavity interaction constants. In three-oscillator model, the eigenstates of Hamiltonian correspond to the three hybrid branches,

the eigenvalues of Hamiltonian correspond to the Hopfield coefficients, and the modular square of Hopfield coefficient represents the proportion of uncoupled states in hybrid state. The diagonalization of these Hamiltonians yields three eigenstates and Hopfield coefficients which present the contribution of plasmons, excitons and microcavity modes to each of the state[52]. With the eigenfrequencies of upper, middle, and lower branches that obtained from experimental reflectivity spectra, the Rabi splitting of anticrossing curves can be fitted with the three-coupled oscillator model. By adjusting the parameters g_{MC} and g_X, and then solving the Hamiltonian, the obtained eigenstates of Hamiltonian can be fitted well with the experimental results.

Figure 4(b) depicts resulting dispersion curves of the Ag-WS$_2$ heterostructure that was embedded in the optical microcavity. Three resonance bands, corresponding to the upper, middle, and lower hybrid states are observed. The extracted values from the fitting give $g_{MC} \approx 90$ meV and $g_X \approx 60$ meV. The splitting between each of two branches depends on both plasmon-exciton (g_X) and plasmon-microcavity (g_{MC}) coupling strengths, as well as the resonant frequency and linewidths of all contributing parts. Thus, the existed analytical expression cannot obtain simple analytical expressions of the eigenfrequencies in this three-coupled oscillator. In order to evaluate the Rabi splitting of the system and find the trigger condition of strong coupling, the weight of each contribution should be estimated.
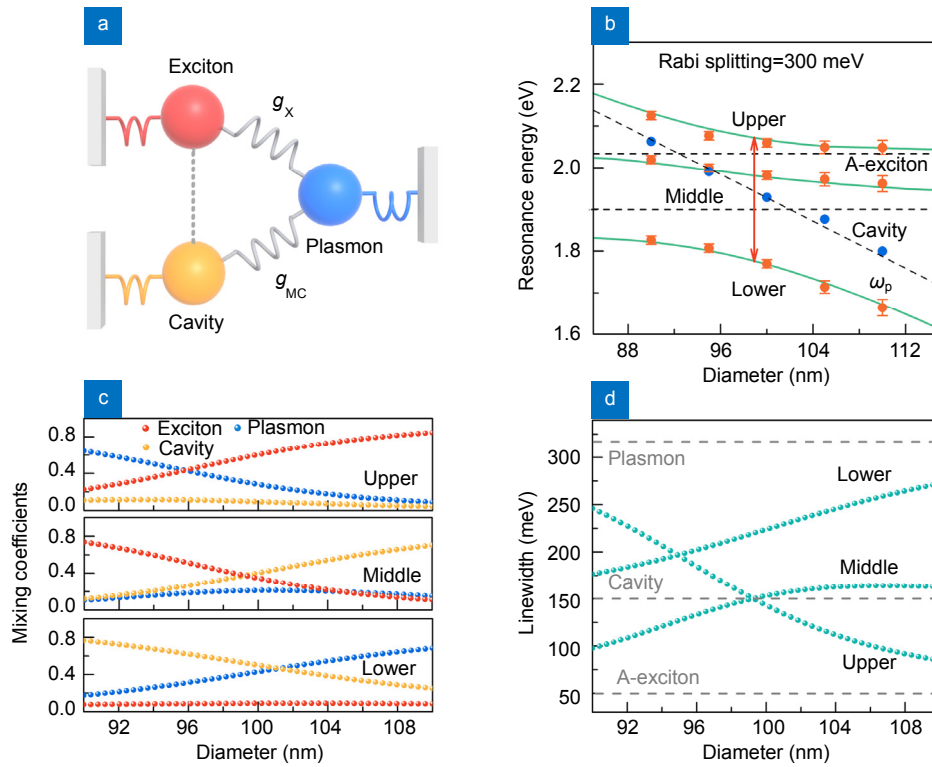
Fig. 4 | Anticrossing behavior of the strong plasmon-exciton-cavity coupling. (a) The three-coupled harmonic oscillator model, which includes the surface plasmons, A-exciton, and microcavity mode as three oscillators. **(b)** Energies of reflectivity dips as a function of the nanodisk diameter extracted from the reflectivity spectrum. Red dots with error bars show energies obtained from the reflectivity spectrum. The horizontal black dashed lines respectively represent the A-exciton and the microcavity resonant energy. The black slanted short-dashed line represents plasmon resonance mode. Three green solid curves correspond to theoretical fits of hybrid branches based on the three-coupled oscillator model. The error bar represents the standard error of a set of measurements. **(c)** Hopfield coefficients for plasmon, exciton, and microcavity contributions to upper, middle, and lower hybrid states as a function of diameter, calculated using the three-coupled oscillator model, which provide the weighting of each constituent. **(d)** Reflectivity spectral linewidths of the upper, middle, and lower branch modes as a function of nanodisk diameter.

As discussed above, the wave function of each hybrid branch is an admixture contribution from the plasmon, cavity and exciton, as $|\psi\rangle = \alpha_{pl}|\text{plasmon}\rangle + \alpha_{MC}|\text{cavity}\rangle + \alpha_{X}|\text{exciton}\rangle$. In order to quantify this hybridization, Hopfield coefficients for three branches were calculated as shown in Fig. 4(c), where we can see that each branch consisted of part-plasmon, part-exciton, and part-cavity modes. For the middle branch, a strong hybridization between A-exciton and plasmon is induced by the coupling of cavity mode. A state with comparable weight of plasmon, cavity and A-exciton ($|\alpha_{pl}|^2 = 0.24$, $|\alpha_{MC}|^2 = |\alpha_{X}|^2 = 0.38$) is obtained at the nanodisk diameter of 99 nm, where all three oscillators intensely participate in the plasmon-exciton-cavity interaction. Therefore, the Ag nanodisk with diameter of 99 nm is considered as the best structure to realize the strongest interaction among these three oscillators, where the corresponding Rabi splitting value Ω 300 meV is obtained.

On the other side, the linewidths of each hybrid branch also consist of the contributed plasmon, exciton, and cavity modes, and can be written as $\gamma_i = \alpha_{pl}\gamma_{pl} + \alpha_{MC}\gamma_{MC} + \alpha_{X}\gamma_{X}$ (i=upper, middle, lower). By putting the linewidths (γ_{pl},

γ_{MC} and γ_{X}) into above formula, the relationship of Ag nanodisk size with the linewidths of three hybrid states can be calculated as shown in Fig. 4(d). In the strongest coupling regime as the Ag nanodisk diameter of 99 nm, the linewidths of upper, middle, and lower branches are γ_{Upper}= 150 meV, γ_{Middle}= 150 meV, and γ_{Lower}= 220 meV. Compared to the strong coupling criterion in two coupled oscillator model, the requirement for strong coupling of three coupled oscillators that according to the contribution of each component (plasmon, exciton, and cavity modes), can be written as $\Omega > W_{pl}\gamma_{pl} + W_{MC}\gamma_{MC} + W_{X}\gamma_{X}$ (see the detailed derivation in Supplementary Information), where W_{pl}, W_{MC}, and W_{X} are the weight of each component in strong plasmon-exciton-cavity coupling, while γ_{pl}, γ_{MC} and γ_{X} are the linewidths of plasmon, exciton, and microcavity modes. After calculating above parameters (Supplementary Information), the obtained minimal splitting between upper and lower branches of 300 meV, satisfies the proposed criterion condition, which demonstrates that the strong plasmon-exciton polaritonic hybrid state is successfully generated by combining the Ag-WS$_2$ heterostructure with the optical microcavity.

Conclusion

In summary, we have successfully shown that a large Rabi splitting can be realized under ambient conditions with a high-quality optical microcavity that participated in the plasmon-exciton coupling. The generated plasmon-exciton polaritonic hybrid states can achieve a corresponding Rabi splitting as 300 meV. By calculating the linewidths and Hopfield coefficient of hybridized modes using harmonic oscillator model, the criteria of the strong coupling for three oscillators was proposed for the first time, and the corresponding large Rabi splitting was achieved in the strong coupling regime of the Ag-WS$_2$ heterostructure that was embedded in the optical microscopy. The proposed three-oscillator configuration provides an effective way to develop the strong coupling effect for the practical applications of plexciton polaritonic device at room temperature based on low dimensional materials.

Experimental section

Growth of WS$_2$ monolayers: Low-pressure chemical vapor deposition (LPCVD) method was employed to grow WS$_2$ monolayers on the sapphire substrate (c-plane of α-Al$_2$O$_3$). Sulfur and tungsten trioxide powders were used as the S and W sources, respectively. A mixture flow of Ar (60 sccm) and H$_2$ (10 sccm) was used as the carrier gas. During the CVD growth processes, the sulfur powder was placed on the upstream zone and heated to 100   . Tungsten trioxide powder and substrate were placed on the middle zone of the tube furnace and heated to 887   with 35 min, and then maintained 60 min for the deposition of the WS$_2$ monolayers. The pressure of the tube furnace was pumped to ~80 Pa. After the growth of WS$_2$, the temperatures were naturally cooled down to room temperature.

Sample fabrication: The substrate was prepared by depositing 100 nm Ag and 30 nm MgF$_2$ successively, which could obviously enhance the optical absorption of WS$_2$ monolayers (Fig. S6, Supplementary Information). The as-grown WS$_2$ monolayers were transferred onto the prepared Ag-MgF$_2$ substrate by a PMMA-assisted method. Then, the designed Ag nanodisks were directly fabricated on WS$_2$ monolayers by E-beam lithography, and there is no spacer between the Ag nanodisk array and the WS$_2$ monolayer. The periods of the Ag nanodisk arrays were set at 230 nm, which makes the surface plasmonic lattice resonances far away from the A-exciton resonance wavelength. Positive resist (MircoChem PMMA A2 950) was spin-coated on the prepared substrate at 3000 rpm for 51 s and then heated on a hot plate for 5 min. The designed structure was drawn by nanometer pattern generation system (NPGS) and exposed by scanning electron microscope (FEI Quanta 450 FEG). A 30 nm Ag film was evaporated by E-beam evaporation system (DE Technology Inc, DE400DH) then lifted off after soaking in acetone for 2 h. Finally, by depositing 155 nm MgF$_2$ and 20 nm Ag, the Ag-WS$_2$ heterostructure with the optical microcavity was achieved.

Simulations and optical measurements: The commercial FDTD solution was used to simulate the optical characterization of strong coupling system. Ag nanodisks with diameter increased from 60 to 130 nm were used to acquire the anti-crossing line shape and the thickness of Ag (up), MgF$_2$ and Ag (bottom) for microcavity analysis was chosen as 20 nm, 185 nm and 100 nm. The refractive index for MgF$_2$ was set as a constant for 1.38. The minimum mesh size for the WS$_2$ monolayers was 0.05 nm and the optical constants for WS$_2$ monolayers were taken from literature and were used without further modification[53]. A non-polarized plane wave with wavelength from 400 to 900 nm was applied as an input source. In the simulation of Fig. 3(c), the monitor of FDTD solutions is located at the interface between the Ag nanodisk and the WS$_2$ monolayer. In the experiment, the reflectivity spectral mapping was obtained by a commercial microscopic imaging system (HIS V3, CytoViva Co.), and the objective lens is 50× magnifications. The reflectivity spectra of the Ag-WS$_2$ heterostructure with and without microcavity were extracted from the mapping images. The whole experiment was operated at room temperature.

References

1. Törmä P, Barnes W L. Strong coupling between surface Plasmon polaritons and emitters: a review. *Rep Prog Phys* **78**, 013901 (2015).
2. Christopoulos S, Von Högersthal G B H, Grundy A J D, Lagoudakis P G, Kavokin A V *et al*. Room-temperature polariton lasing in semiconductor microcavities. *Phys Rev Lett* **98**, 126405 (2007).
3. Kasprzak J, Richard M, Kundermann S, Baas A, Jeambrun P *et al*. Bose–Einstein condensation of exciton polaritons. *Nature* **443**, 409–414 (2006).
4. Deng H, Haug H, Yamamoto Y. Exciton-polariton Bose-Einstein condensation. *Rev Mod Phys* **82**, 1489–1537 (2010).
5. Plumhof J D, Stöferle T, Mai L J, Scherf U, Mahrt R F. Room-temperature Bose–Einstein condensation of cavity exciton–polaritons in a polymer. *Nat Mater* **13**, 247–252 (2014).
6. Hutchison J A, Schwartz T, Genet C, Devaux E, Ebbesen T W. Modifying chemical landscapes by coupling to vacuum fields. *Angew Chem Int Edit* **51**, 1592–1596 (2012).
7. Galego J, Garcia-Vidal FJ, Feist J. Suppressing photochemical reactions with quantized light fields. *Nat Commun* **7**, 13841 (2016).
8. Shi X, Ueno K, Oshikiri T, Sun Q, Sasaki K *et al*. Enhanced water splitting under modal strong coupling conditions. *Nat Nanotechnol* **13**, 953–958 (2018).
9. Amo A, Liew T C H, Adrados C, Houdré R, Giacobino E *et al*. Exciton–polariton spin switches. *Nat Photonics* **4**, 361–366 (2010).
10. Peter E, Senellart P, Martrou D, Lemaître A, Hours J *et al*. Exciton-photon strong-coupling regime for a single quantum dot

embedded in a microcavity. *Phys Rev Lett* **95**, 067401 (2005).

11. Baumberg J J, Kavokin A V, Christopoulos S, Grundy A J D, Butté R *et al*. Spontaneous polarization buildup in a room-temperature polariton laser. *Phys Rev Lett* **101**, 136409 (2008).

12. Li F, Orosz L, Kamoun O, Bouchoule S, Brimont C *et al*. From excitonic to photonic polariton condensate in a ZnO-based microcavity. *Phys Rev Lett* **110**, 196406 (2013).

13. Kéna-Cohen S, Forrest S R. Room-temperature polariton lasing in an organic single-crystal microcavity. *Nat Photonics* **4**, 371–375 (2010).

14. Agranovich V M, Litinskaia M, Lidzey D G. Cavity polaritons in microcavities containing disordered organic semiconductors. *Phys Rev B* **67**, 085311 (2003).

15. Mak K F, Lee C, Hone J, Shan J, Heinz T F. Atomically thin MoS$_2$: a new direct-gap semiconductor. *Phys Rev Lett* **105**, 136805 (2010).

16. Wang Q H, Kalantar-Zadeh K, Kis A, Coleman J N, Strano M S. Electronics and optoelectronics of two-dimensional transition metal dichalcogenides. *Nat Nanotechnol* **7**, 699–712 (2012).

17. Ramasubramaniam A. Large excitonic effects in monolayers of molybdenum and tungsten dichalcogenides. *Phys Rev B* **86**, 115409 (2012).

18. Qiu D Y, da Jornada F H, Louie S G. Optical spectrum of MoS$_2$: many-body effects and diversity of exciton states. *Phys Rev Lett* **111**, 216805 (2013).

19. Liu X Z, Galfsky T, Sun Z, Xia F N, Lin E C *et al*. Strong light–matter coupling in two-dimensional atomic crystals. *Nat Photonics* **9**, 30–34 (2015).

20. Sun Z, Gu J, Ghazaryan A, Shotan Z, Considine C R *et al*. Optical control of room-temperature valley polaritons. *Nat Photonics* **11**, 491–496 (2017).

21. Chen Y J, Cain J D, Stanev T K, Dravid V P, Stern N P. Valley-polarized exciton–polaritons in a monolayer semiconductor. *Nat Photonics* **11**, 431–435 (2017).

22. Barnes W L, Dereux A, Ebbesen T W. Surface plasmon subwavelength optics. *Nature* **424**, 824–830 (2003).

23. Vasa P, Wang W, Pomraenke R, Lammers M, Maiuri M *et al*. Real-time observation of ultrafast Rabi oscillations between excitons and plasmons in metal nanostructures with J-aggregates. *Nat Photonics* **7**, 128–132 (2013).

24. Väkeväinen A I, Moerland R J, Rekola H T, Eskelinen A P, Martikainen J P *et al*. Plasmonic surface lattice resonances at the strong coupling regime. *Nano Lett* **14**, 1721–1727 (2014).

25. Shi L, Hakala T K, Rekola H T, Martikainen J P, Moerland R J *et al*. Spatial coherence properties of organic molecules coupled to plasmonic surface lattice resonances in the weak and strong coupling regimes. *Phys Rev Lett* **112**, 153002 (2014).

26. Rodriguez S R K, Feist J, Verschuuren M A, Garcia Vidal F J, Gómez Rivas J. Thermalization and cooling of plasmon-exciton polaritons: towards quantum condensation. *Phys Rev Lett* **111**, 166802 (2013).

27. Hägglund C, Zeltzer G, Ruiz R, Wangperawong A, Roelofs K E *et al*. Strong coupling of plasmon and nanocavity modes for dual-band, near-perfect absorbers and ultrathin photovoltaics. *ACS Photonics* **3**, 456–463 (2016).

28. Yang J H, Sun Q, Ueno K, Shi X, Oshikiri T *et al*. Manipulation of the dephasing time by strong coupling between localized and propagating surface Plasmon modes. *Nat Commun* **9**, 4858 (2018).

29. Shi J W, Lin M H, Chen I T, Estakhri N M, Zhang X Q *et al*. Cascaded exciton energy transfer in a monolayer semiconductor lateral heterostructure assisted by surface Plasmon polariton. *Nat Commun* **8**, 35 (2017).

30. Wang M S, Li W, Scarabelli L, Rajeeva B B, Terrones M *et al*. Plasmon–trion and Plasmon–exciton resonance energy transfer from a single plasmonic nanoparticle to monolayer MoS$_2$. *Nanoscale* **9**, 13947–13955 (2017).

31. Wang Z, Dong Z G, Gu Y H, Chang Y H, Zhang L *et al*. Giant photoluminescence enhancement in tungsten-diselenide-gold plasmonic hybrid structures. *Nat Commun* **7**, 11283 (2016).

32. Sobhani A, Lauchner A, Najmaei S, Ayala-Orozco C, Wen F F *et al*. Enhancing the photocurrent and photoluminescence of single crystal monolayer MoS$_2$ with resonant plasmonic nanoshells. *Appl Phys Lett* **104**, 031112 (2014).

33. Butun S, Tongay S, Aydin K. Enhanced light emission from large-area monolayer MoS$_2$ using plasmonic nanodisc arrays. *Nano Lett* **15**, 2700–2704 (2015).

34. Gao W, Lee Y H, Jiang R B, Wang J F, Liu T X *et al*. Localized and continuous tuning of monolayer MoS$_2$ photoluminescence using a single shape- controlled Ag nanoantenna. *Adv Mater* **28**, 701–706 (2016).

35. Janisch C, Song H M, Zhou C J, Lin Z, Elías A L *et al*. MoS$_2$ monolayers on nanocavities: enhancement in light–matter interaction. *2D Mater* **3**, 025017 (2016)

36. Hao Q, Pang J B, Zhang Y, Wang J W, Ma L B *et al*. Boosting the photoluminescence of monolayer MoS$_2$ on high- density nanodimer arrays with sub-10 nm gap. *Adv Opt Mater* **6**, 1700984 (2018).

37. Sun J W, Hu H T, Zheng D, Zhang D X, Deng Q *et al*. Light-emitting plexciton: exploiting Plasmon–exciton interaction in the intermediate coupling regime. *ACS Nano* **12**, 10393–10402 (2018).

38. Lee B, Park J, Han G H, Ee H S, Naylor C H *et al*. Fano resonance and spectrally modified photoluminescence enhancement in monolayer MoS$_2$ integrated with plasmonic nanoantenna array. *Nano Lett* **15**, 3646–3653 (2015).

39. Li B W, Zu S, Zhou J D, Jiang Q, Du B W *et al*. Single-nanoparticle plasmonic electro-optic modulator based on MoS$_2$ monolayers. *ACS Nano* **11**, 9720–9727 (2017).

40. Wang M S, Krasnok A, Zhang T Y, Scarabelli L, Liu H *et al*. Tunable fano resonance and Plasmon-exciton coupling in single Au nanotriangles on monolayer WS$_2$ at room temperature. *Adv Mater* **30**, 1705779 (2018).

41. Chikkaraddy R, de Nijs B, Benz F, Barrow S J, Scherman O A *et al*. Single-molecule strong coupling at room temperature in plasmonic nanocavities. *Nature* **535**, 127–130 (2016).

42. Wang S J, Li S L, Chervy T, Shalabney A, Azzini S *et al*. Coherent coupling of WS$_2$ monolayers with metallic photonic nanostructures at room temperature. *Nano Lett* **16**, 4368–4374 (2016).

43. Zheng D, Zhang S P, Deng Q, Kang M, Nordlander P *et al*. Manipulating coherent Plasmon-exciton interaction in a single silver nanorod on monolayer WSe$_2$. *Nano Lett* **17**, 3809–3814 (2017).

44. Wen J X, Wang H, Wang W L, Deng Z X, Zhuang C *et al*. Room-temperature strong light–matter interaction with active control in single plasmonic nanorod coupled with two-dimensional atomic crystals. *Nano Lett* **17**, 4689–4697 (2017).

45. Lee B, Liu W J, Naylor C H, Park J, Malek S C *et al*. Electrical tuning of exciton-Plasmon polariton coupling in monolayer MoS$_2$

integrated with plasmonic nanoantenna lattice. *Nano Lett* **17**, 4541–4547 (2017).

46. Cuadra J, Baranov D G, Wersäll M, Verre R, Antosiewicz T J *et al*. Observation of tunable charged exciton polaritons in hybrid monolayer WS$_2$-plasmonic nanoantenna system. *Nano Lett* **18**, 1777–1785 (2018).

47. Wurdack M, Lundt N, Klaas M, Baumann V, Kavokin A V *et al*. Observation of hybrid Tamm-Plasmon exciton- polaritons with GaAs quantum wells and a MoSe$_2$ monolayer. *Nat Commun* **8**, 259 (2017).

48. Chakraborty B, Gu J, Sun Z, Khatoniar M, Bushati R *et al*. Control of strong light–matter interaction in monolayer WS$_2$ through electric field gating. *Nano Lett* **18**, 6455–6460 (2018).

49. Schuller J A, Barnard E S, Cai W S, Jun Y C, White J S *et al*. Plasmonics for extreme light concentration and manipulation. *Nat Mater* **9**, 193–204 (2010).

50. Chanda D, Shigeta K, Truong T, Lui E, Mihi A *et al*. Coupling of plasmonic and optical cavity modes in quasi-three-dimensional plasmonic crystals. *Nat Commun* **2**, 479 (2011).

51. Ameling R, Giessen H. Cavity plasmonics: large normal mode splitting of electric and magnetic particle plasmons induced by a photonic microcavity. *Nano Lett* **10**, 4394–4398 (2010).

52. Hopfield J J. Theory of the contribution of excitons to the complex dielectric constant of crystals. *Phys Rev* **112**, 1555–1567 (1958).

53. Li Y L, Chernikov A, Zhang X, Rigosi A, Hill H M *et al*. Measurement of the optical dielectric function of monolayer transition-metal dichalcogenides: MoS$_2$, MoSe$_2$, WS$_2$, and WSe$_2$. *Phys Rev B* **90**, 205422 (2014).

Competing interests

The authors declare no competing financial interests.

Supplementary information

Supplementary information for this paper is available at https://doi.org/10.29026/oea.2019.190008